



Minerva Access is the Institutional Repository of The University of Melbourne

**Author/s:**

Shi, S;Lam, N;Cui, Y;Lu, G;Gad, E;Zhang, L

**Title:**

Indentation modelling of aluminium cladding panels subjected to hailstone impact

**Date:**

2023-09

**Citation:**

Shi, S., Lam, N., Cui, Y., Lu, G., Gad, E. & Zhang, L. (2023). Indentation modelling of aluminium cladding panels subjected to hailstone impact. *International Journal of Impact Engineering*, 179, <https://doi.org/10.1016/j.ijimpeng.2023.104638>.

**Persistent Link:**

<https://hdl.handle.net/11343/332562>



## 22 **1. Introduction**

23 A hailstorm event can inflict a considerable amount of damage to the cladding panels of a  
24 building. A cladding panel that has been impacted by hailstones may have its surface defaced  
25 requiring replacement. The replacement bills on damaged buildings in a city in the aftermath  
26 of a hailstorm can be up to tens of millions of dollars [1-3]. Should the storm intensity be severe  
27 enough to cause perforation of the panel allowing the ingress of water, colossal damage can be  
28 caused to the interior of the building and its contents [4, 5]. An accurate, and reliable, analytical  
29 method for predicting the extent of damage to cladding panels would serve the purpose of  
30 setting insurance premiums to fairly distribute risks, and providing realistic hazard assessments  
31 to guide decision making for optimising preventive measures.

32 Knowledge on damage prediction of impact actions is not commonly shared amongst building  
33 professionals. Realistic assessment of the risk of damage would need to involve resolving an  
34 impact action into two components: (1) global impulsive action and (2) localised contact action.  
35 The amount of deflection of a structural element caused by the impact of a heavy moving object  
36 is controlled by impulsive action. The prediction of the amount of deflection sustained by the  
37 element can be based on equal momentum and energy principles [6-9]. This analytical  
38 methodology, which is suited to dealing with the impact of a heavy moving impactor, gives  
39 more accurate predictions than the code stipulated equivalent quasi-static force method or the  
40 equal energy method [10]. However, the impact of a flying projectile, or a hailstone, on a  
41 cladding panel is more complex because of its highly transient and localised nature. With this  
42 type of impact scenario, the inflicted damage is more to do with the amount of force  
43 experienced at the point of contact on the surface of the panel (referred to herein as “contact  
44 force”). Quantification of contact force has been studied and reported [11-18]. Investigations  
45 into the impact resistance of different types of cladding products or metal panels such as roof  
46 sheeting [19], composite panels [20-24], and steel plates [25, 26], have also been reported in

47 the literature. However, no analytical predictive model for the impact by hail has been  
48 developed. Thus, little is known of the amount of indentation that can be caused by hail impact  
49 into an aluminium alloy panel which is a common type of installation in contemporary  
50 buildings.

51 Sophisticated finite element (FE) software packages such as ABAQUS and LS-DYNA have  
52 been used to simulate complex interactions between the ice specimen (the impactor) and the  
53 surface of the test panel (the target) [27-29]. Advanced computational algorithms such as ALE,  
54 and SPH, are claimed to be able to model the mechanical behaviour of the ice impactor [30-  
55 33]. An important drawback with these simulation tools is that despite being validated by  
56 experimental measurements, inconsistencies in their abilities to predict the same scenario have  
57 been revealed among some of the published models [34]. Another important drawback of the  
58 numerical simulation methodology in the context of day-to-day design practice is the high  
59 demand for memory and computational time. The high computational cost is compounded by  
60 the need for repetitive executions to achieve convergence. From the users' perspectives in the  
61 context of day-to-day engineering practices, an experimentally validated analytical model is  
62 much preferred to numerical (FE) models.

63 Plastic deformation of a metal plate has been studied extensively since the last century [35].  
64 Investigations have been undertaken to predict irrecoverable transverse displacement when  
65 subject to impulsive actions [36-39]. Membrane theory has been used to expedite the analysis  
66 of a thin plate in response to an out of plane impact action [39-41]. Note, this type of analysis  
67 is only valid if the amount of indentation relative to the thickness of the panel is large.  
68 Analytical modelling for predicting permanent indentation into an aluminium alloy panel has  
69 been treated in a few investigations [40-44]. Permanent indentation into the surface of an  
70 aluminium panel was of interest in one of these studies [45]. However, the impact actions  
71 considered in these cited references were not specific to hail impact which is unique in the

72 sense that the inflicted damage to the panel is very localised. With the impact by hailstones on  
73 claddings, the amount of indentation can be small in comparison with the thickness of the  
74 cladding in order that simplifications by membrane theory cannot be applied.

75 The original contribution of this study is the development of an analytical model for predicting  
76 the amount of permanent indentation caused by hail impact into the surface of a (cladding)  
77 panel made of aluminium alloy. Strain rate effects and contributions from both the membrane  
78 and flexural actions have been incorporated in the derivation of the predictive expressions. The  
79 schematic diagram of Fig. 1 shows different stages of a hail impacting an aluminium panel,  
80 along with typical measurements of the contact force, strain, and displacement at the impact  
81 point, as observed from impact experiments conducted in this study. Stage A is the time  
82 instance when the ice impactor makes initial contact with the surface of the aluminium panel.  
83 In less than half a millisecond, the magnitude of the contact force and the in-plane strain  
84 increased monotonically with time prior to reaching the peak (Stage B). In experiments  
85 conducted by the authors, cracks were observed to have propagated fully into the ice specimen  
86 whilst localised indentation was formed in the aluminium panel. As the ice impactor  
87 experienced disintegration and fragmentation, both the contact force and direct strain gradually  
88 decreased back to zero. The global displacement of the plate, which took a much longer time  
89 to react, eventually reached its fullest extent long afterwards (Stage C). The global response of  
90 the plate which consisted mainly of elastic deflection and vibration eventually diminished  
91 through energy dissipation by damping. In the end, permanent indentation was found at the  
92 contact region (Stage D).

93 The accuracy of the proposed analytical model has been validated by comparison against  
94 results from 37 impact tests conducted by the authors. Both the analytical and experimental  
95 work presented in this article are original. To fulfil the stated project aim through impact

96 experimentation (the details of which are presented in Section 2), investigations were directed  
97 at the following topics:

98 I. Strain development time histories (Section 3.1) and strain rate effects (Section 3.2)

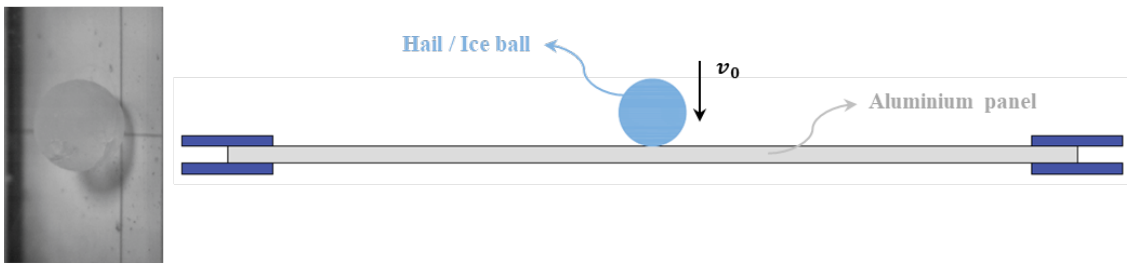
99 II. Indentation profile modelling (Section 3.3)

100 III. Permanent indentation estimates (Section 4.1)

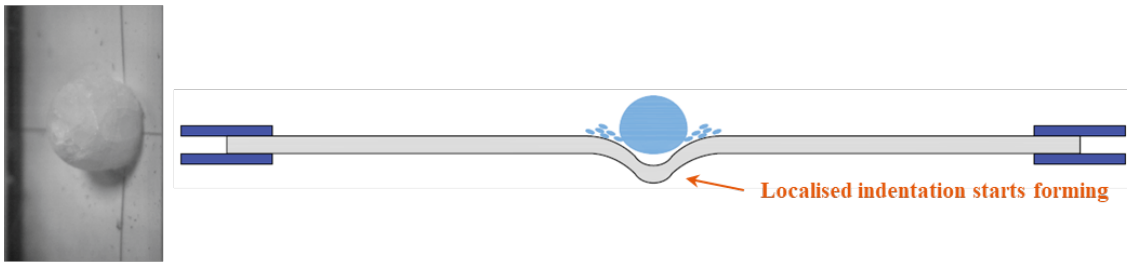
101 IV. Experimental validation of the accuracy of model predictions (Section 4.2)

102 V. Example application of model (Section 5)

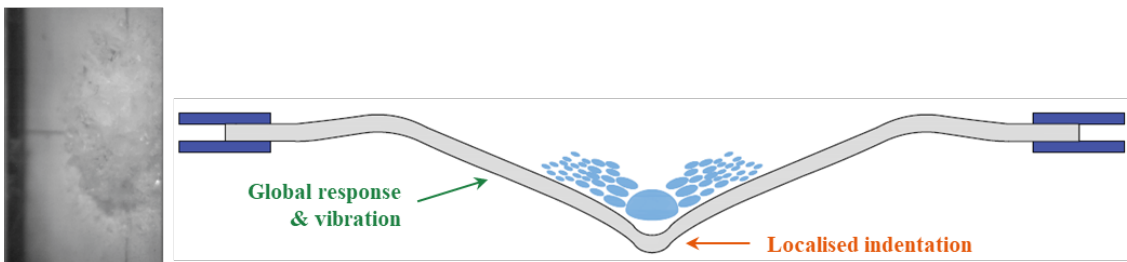
**A. Commencement of impact**



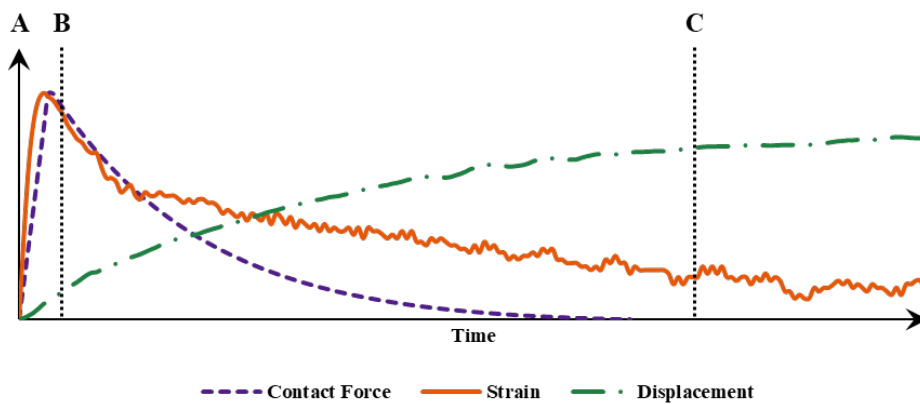
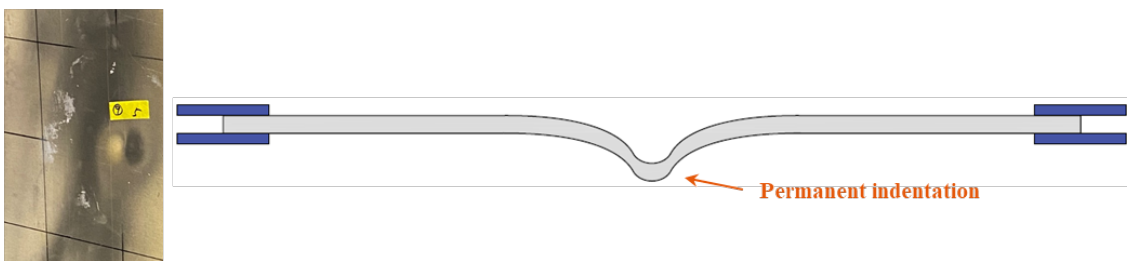
**B. Maximum strain**



**C. Maximum displacement**



**D. Post-impact**



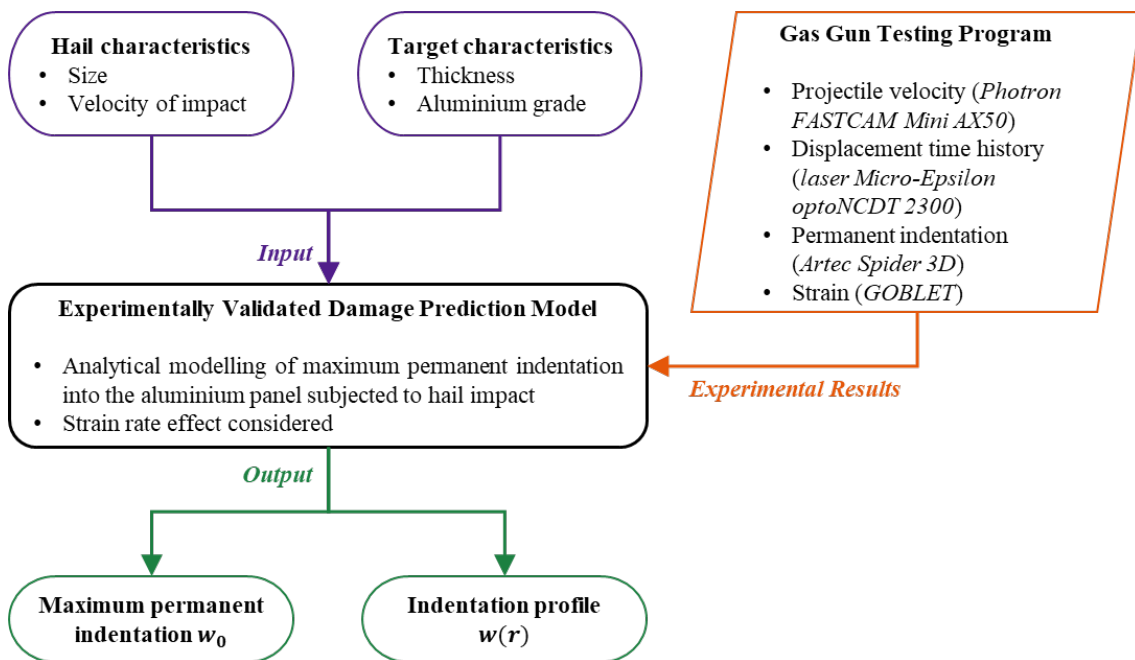
103

104  
105

Fig. 1. Schematic diagrams showing different stages of a hail impacting an aluminium panel and typical measurements of contact force, strain and displacement at the impact point.

106 **2. Experimental Investigation**

107 This section presents details of the testing program which involved the use of the gas gun  
 108 accelerating ice impactors onto a specimen of the aluminium cladding. A total of 37 tests were  
 109 performed and recorded, with the velocity of impact ranging from ~35 m/s to ~80 m/s.  
 110 Observations and measurements from the full-scale impact experimentation provided valuable  
 111 guidance in developing and validating the proposed damage prediction model, as presented  
 112 schematically in Fig. 2.



113

114 **Fig. 2. A schematic overview of the framework of the developed analytical model in this study.**

115

116 **2.1. Spherical ice impactor**

117 Spherical ice impactors with a diameter of 50.8 mm were fabricated for use in the impact tests.  
 118 The size of these ice specimens was at the upper limit employed for impact testing of roofing  
 119 panels for hail resistance according to relevant regulatory documents (ANSI/FM\_4473 2011).  
 120 To ensure that the specimens were free of cracks and air bubbles, vacuum-insulated cylindrical  
 121 containers were used to facilitate top-down freezing [17, 18]. Ice cylinders frozen inside the

122 insulated containers were then melted using a custom-designed ice mould as shown in Fig. 3(a).  
123 The spherical mould was initially divided into two halves which were separated by the (slightly  
124 oversized) ice specimen. As the ice started to melt, the two halves of the mould came closer  
125 whilst forcing the ice into a sphere. A micro lever switch which was connected to a light bulb  
126 and an alarm was attached to the side of the mould to give signals to the user as soon as the  
127 two halves came in contact. This manner of moulding the ice specimen facilitates uniform  
128 cooling and avoids the formation of any air voids, or imperfections, as shown in Fig. 3(b).  
129 Testing with void-and-imperfection-free ice impactors has the benefit of making the  
130 experimental results repeatable in order to ensure a fair comparison with the deterministic  
131 model predictions.



(a)

(b)

134 **Fig. 3. Preparation of ice ball impactor: (a) a custom-designed ice mould for forming spherical ice**  
135 **specimen (b) a clear ice ball free of cracks for the impact test.**

136

## 137 **2.2. Aluminium alloy panel specimen**

138 Aluminium panels (alloy 5083-H116) with planar dimensions of 1000 mm × 1000 mm and  
139 thicknesses of 3 mm and 4 mm were employed for the testing. The exposed area of the panel  
140 was 900 mm × 900 mm. Typically, cladding panels made of aluminium alloy with a thickness

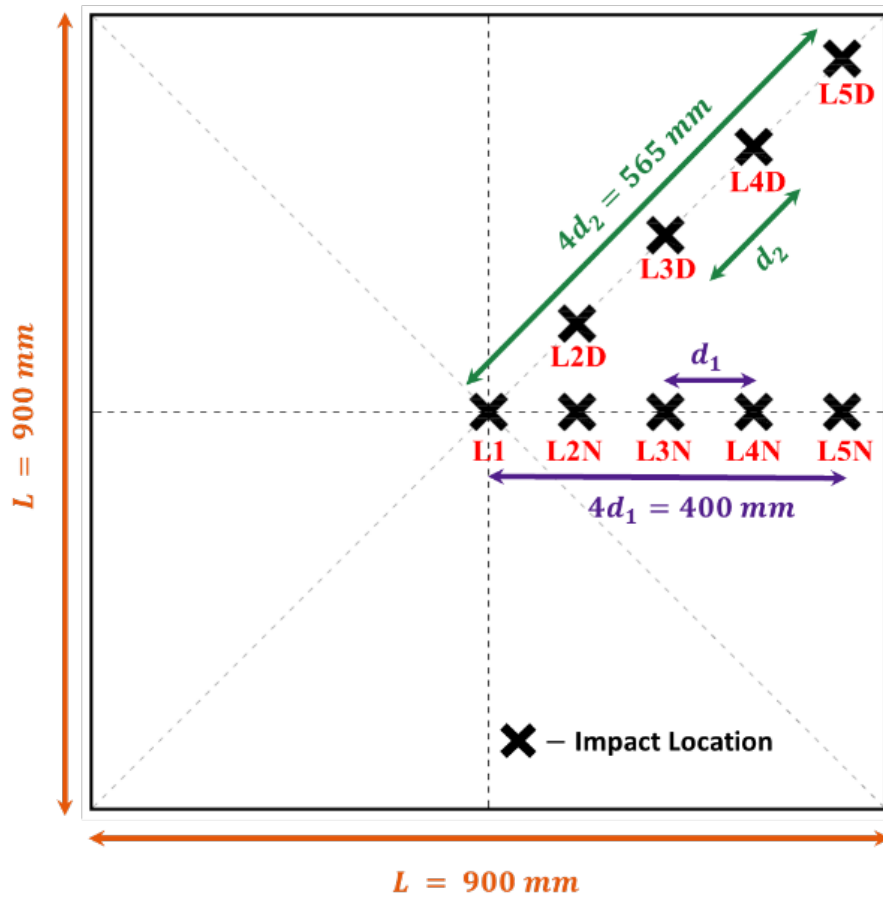
141 of 3 mm or 4 mm are used in the global market. It is rare to see aluminium alloy cladding panels  
 142 with larger thicknesses, except for sandwich panels which has a honeycomb structure as the  
 143 core. Thinner panels are not recommended as they are prone to large deformations from intense  
 144 impact by hailstones and windborne debris. Selection of the cladding panel specimen was  
 145 guided by professional industrial advice [46] in which a standard panel with exposed dimension  
 146 of 900 mm × 900 mm is specified. The analytical model presented in Section 4 has been  
 147 validated by experimental results obtained from panels which are either 3 mm or 4 mm thick.  
 148 By energy principles (as described in Section 4.1) the developed model is applicable to panels  
 149 of different thicknesses.

150 In the impact tests, the panel specimen was struck at designated positions at 100 mm spacings  
 151 along two straight lines in both the normal and diagonal directions as shown in Fig. 4(a). A  
 152 photo taken from the panel specimen which was mounted on the test frame is shown in Fig.  
 153 4(b). The relevant material properties of the aluminium panels are listed in Table 1. The idea  
 154 of having the test specimen impacted at multiple locations was to study the spatial variation of  
 155 permanent indentation within the panel as commonly observed [46].

156 **Table 1: Material properties of target aluminium panels samples with 3 mm and 4 mm thickness,**  
 157 **respectively (ASTM B928M).**

Alloy grade	Density ( $kg/m^3$ )	Elastic Modulus ( $GPa$ )	Yield Strength ( $MPa$ )	Dimensions ( $mm$ )
Aluminium 5083-H116	2660	71	215	900 × 900 × <b>3 (THK)</b> OR 900 × 900 × <b>4 (THK)</b>

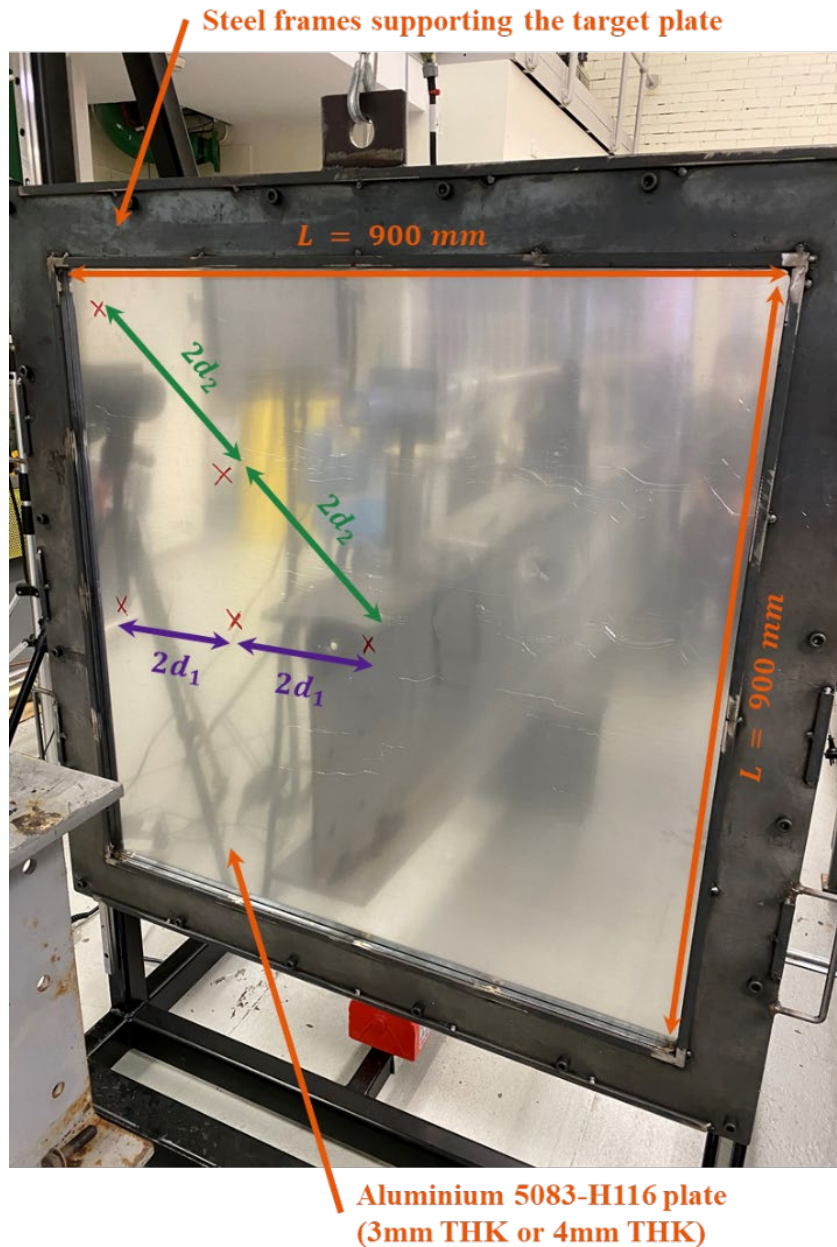
158



159

160

(a)



161

162 Fig. 4. (a) A schematic drawing of the panel specimen and locations of impact (b) a photo of one panel  
 163 sample used in the impact test.

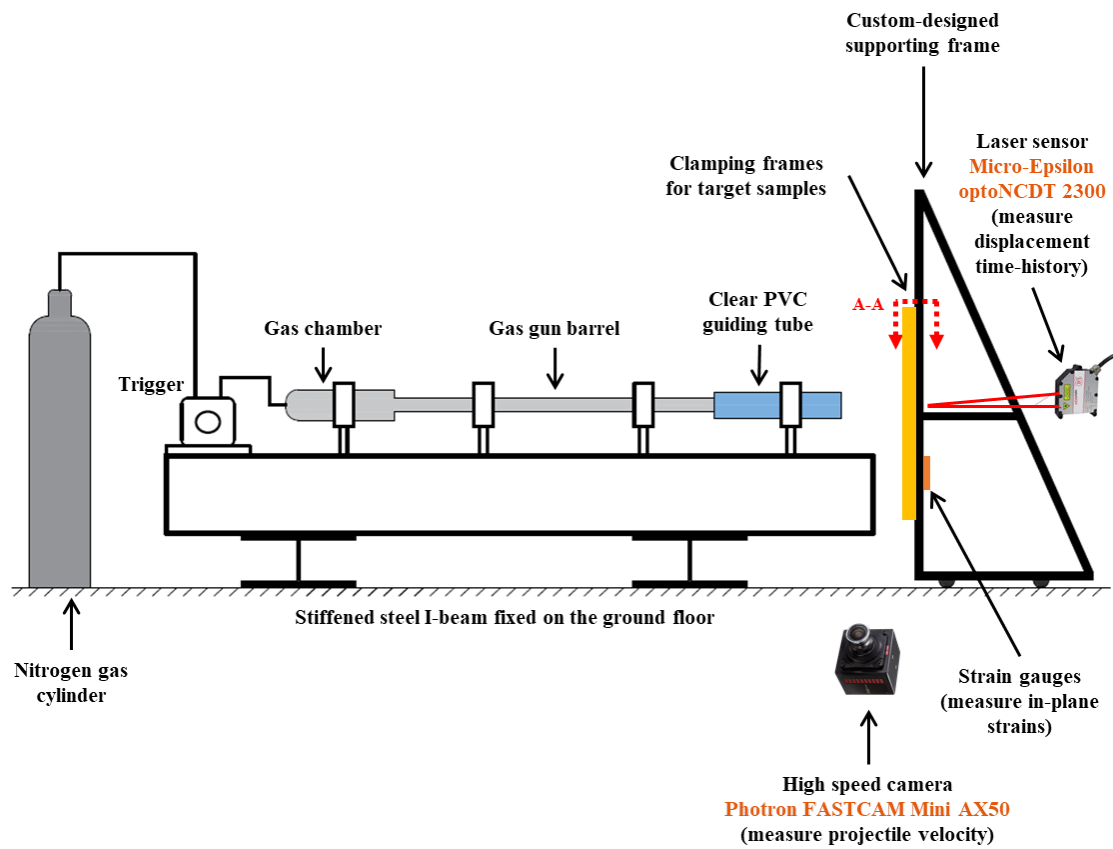
164

165 **2.3. Setup of the gas gun testing**

166 The experimental setup which is schematically shown in Fig. 5(a) features the use of  
 167 compressed nitrogen gas for accelerating the ice impactor onto an aluminium panel which was  
 168 supported by a custom-designed steel frame. The aluminium panel was sandwiched in between

169 two steel frames (10 mm in thickness) which were bolted together, representing a fully clamped  
170 boundary condition along the edges (Fig. 5(b)). The steel frame as shown in Fig. 6(a), was  
171 equipped with linear bearings and rails and an electric motor to give allowance for a full range  
172 of vertical movement. The black triangular stand, with wheels and sliding rails at the bottom,  
173 enabled the targeted panel to freely slide in the horizontal direction. The spherical ice impactor  
174 was launched through a steel gun barrel which was connected to a PVC guiding pipe to  
175 effectively minimise the melting of the ice specimen during launching. The incident velocity  
176 of impact of the ice projectile was measured using a high-speed camera (*Photron FASTCAM*  
177 *Mini AX50*) which was positioned in close proximity to the frontal surface of the targeted panel.  
178 The shooting angle was perpendicular to the direction of the projectile to improve measurement  
179 accuracy. The high-speed camera was set at 37,500 frames per second to capture images during  
180 the course of the impact. A laser sensor (*Micro-Epsilon optoNCDT-2300*) was also positioned  
181 at the rear side of the panel to record the displacement time history at the impact position. The  
182 laser sensor was securely fastened on the stationary steel I-beam and adjusted to align with the  
183 centreline of the gas gun barrel for a precise measurement at the impact position. Displacement  
184 signals were measured at a sampling frequency of 20 kHz over a measurement range of 300  
185 mm. Multiple strain gauges were attached at both the front and back side of the panel specimen  
186 for measuring the in-plane strain time histories, as shown in Fig. 6(b) (these strain gauges had  
187 gauge factor of 2.13, resistance of 120  $\Omega$  and were connected to a *Wheatstone Bridge* with  
188 quarter-bridge configuration). The voltage signal from the bridge connection was first  
189 amplified and then recorded by an oscilloscope (*Tektronix TBS 2000B*) at a sampling frequency  
190 of 1 MHz. The triggering of the data acquisition was initiated by the laser sensor (edge trigger  
191 with a falling slope), and then synchronised with the high-speed camera and strain gauges to  
192 ensure consistency in the recorded timeframe. As the testing was completed, an optical 3D

193 scanner (*Artec Spider 3D*) was employed to measure the indentation profile of the damaged  
194 panel.

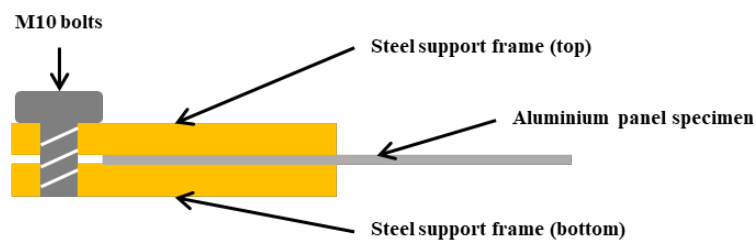


195

196

(a)

Cross section A-A view (boundary fixture detail):



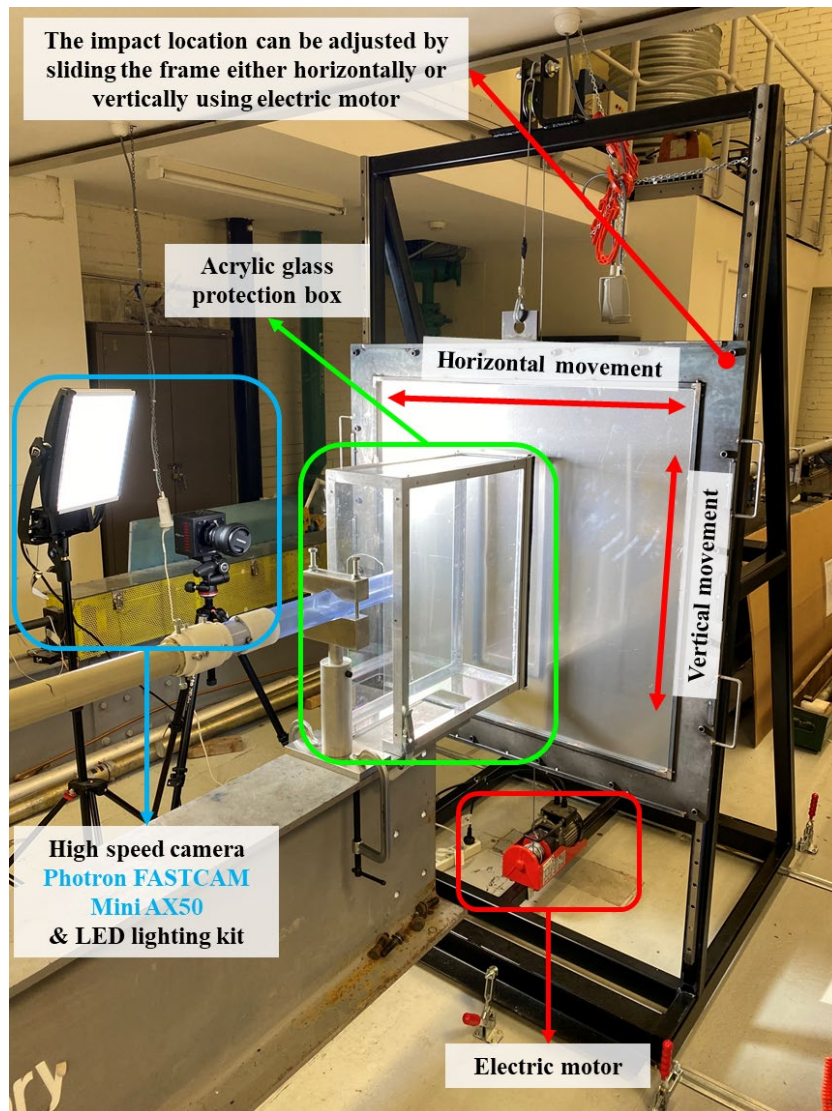
197

198

(b)

199 Fig. 5. (a) A schematic diagram of the experimental apparatus used in the impact test (b) zoom-in view of  
200 the boundary fixture details of the target panel.

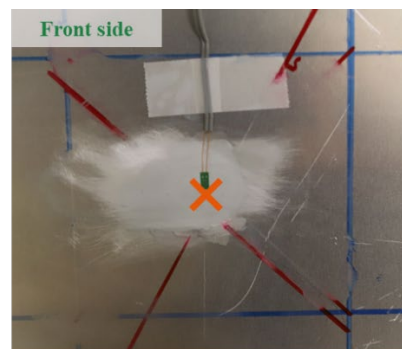
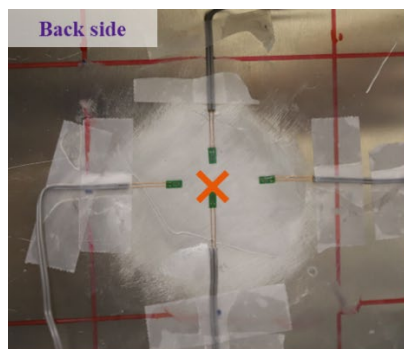
201



202

203

(a)



204

✗ Impact point

✗ Impact point

205

(b)

(c)

206 Fig. 6. (a) Photo of the experimental setup (b) photo showing the arrangement of strain gauges at the back side of the tested panel, strain gauges were attached with a distance of 0, 10, 15, and 20 mm away from  
 207 the impact point (c) photo showing the arrangement of strain gauge at the front side of the tested panel,  
 208 strain gauge was attached at the impact point.  
 209

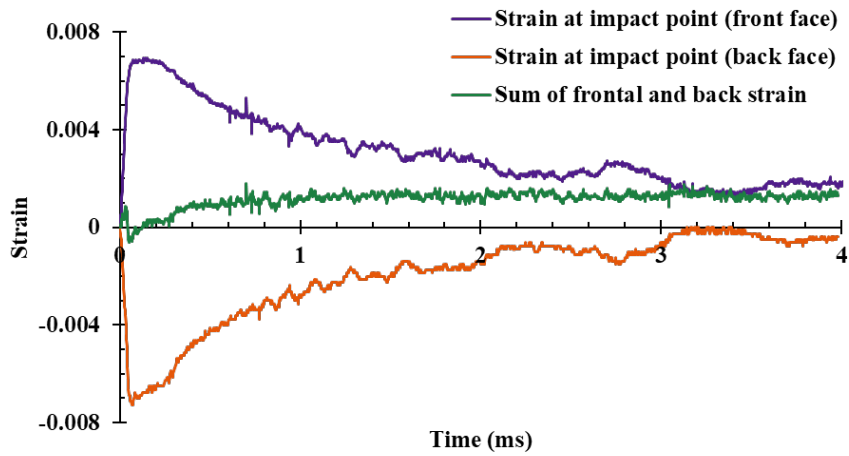
## 210 **3. Testing Results**

### 211 **3.1. Strain time histories and timing of occurrence of permanent indentation**

212 Strain gauges were attached to both sides of the panel to capture the rapid change in strains  
213 experienced by the specimen at the point of impact. Fig. 7(a) shows a typical record of the  
214 strain time histories which show that the surface strain at the front side of the panel (purple  
215 curve) was nearly symmetrical to that at the backside (orange curve). The summation of strains  
216 measured from both sides (green curve) was very small ( $\sim 0$ ) throughout the event, indicating  
217 that the neutral axis remained to be very close to the midplane of the plate implying little axial  
218 stresses. This observation has the important implication that the amount of membrane action  
219 was negligible (which was one of the assumptions made when developing the analytical model).

220 Overlaying the recorded displacement time history on the strain time history Fig. 7(b) reveals  
221 the timing of the formation of the permanent indentation. The occurrence of the peak strain ( $\sim$   
222 0.1 ms) was considerably earlier than the occurrence of the maximum displacement ( $\sim 3$  ms)  
223 and is consistent with the behaviour as shown in the schematic diagrams of Fig. 1. For the  
224 impact scenarios considered in this study, the yield strain ( $\epsilon_y$ ) is approximately 0.0042 ( $\epsilon_y =$   
225  $\sigma_d/E = 297 \text{ MPa}/71 \text{ GPa} \approx 0.0042$ ; refer to Section 3.2 for more details), as shown by the  
226 annotation in Fig. 7(b). It can be inferred from the recorded time histories that irrecoverable  
227 indentation of the aluminium plate was fully formed in the first 1 ms, which was well before  
228 the deflection of the panel reaching its peak. It is also evident that there was no significant  
229 further increase in the amount of deformation after 1 ms, and no increase at all after 2 ms. The  
230 rapid fragmentation of ice upon impact has resulted in a rapid reduction in the stress  
231 concentration. As a result, the development of the localised stress and that of membrane action  
232 occurred at different times. Had the impactor been made of metal or other materials that would

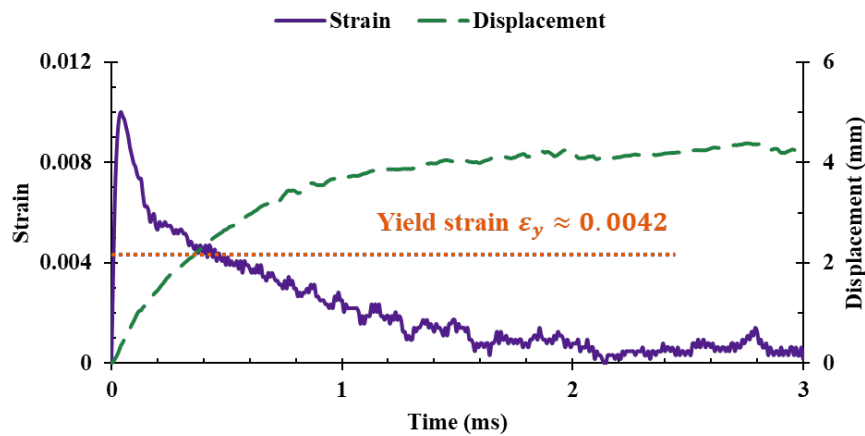
233 remain intact during the collision, highly localised stress concentration would have lasted much  
234 longer thereby co-existing with membrane action in the vicinity of the impactor.



235

236

(a)



237

238

(b)

239 Fig. 7. (a) Experimentally measured strain time histories at the point of impact from the strain gauges  
240 attached at the front and the back side of the plate (b) experimentally measured strain and displacement  
241 time histories at the point of impact.

242

### 243 3.2. Mean strain rate and dynamic flow stress

244 The effect of strain rate should not be overlooked in the context of an impact scenario as  
245 considered in this study. Mean dynamic flow stress  $\sigma_d$  is introduced herein based on the

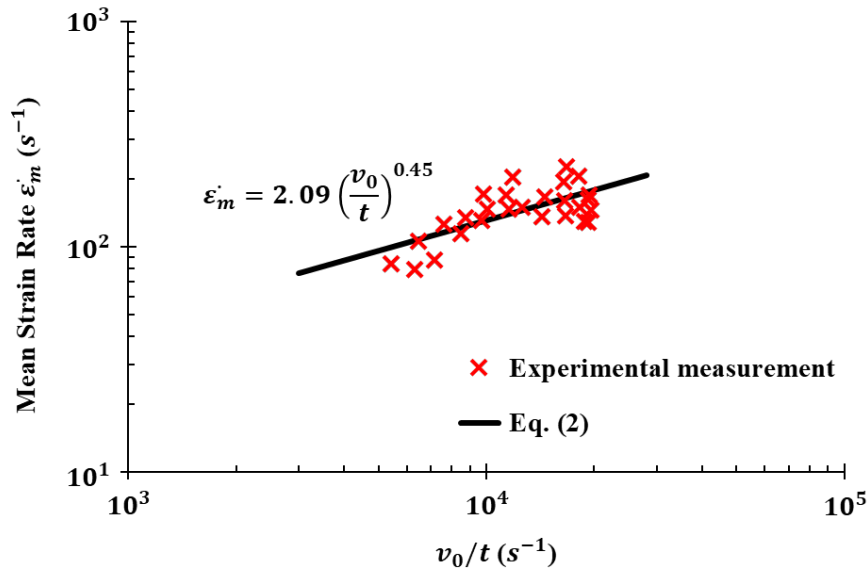
246 assumption of established flow relationships and Tresca yield criterion for rigid plastic material  
247 [47] which can be expressed in the form of the Cowper-Symonds equation as shown in Eq. (1).

$$248 \quad \sigma_d = \sigma_y \left[ 1 + \left( \frac{\dot{\epsilon}_m}{D} \right)^{\frac{1}{q}} \right] \quad (1)$$

249 where,  $\sigma_y$  is the yield stress of the aluminium alloy,  $\dot{\epsilon}_m$  is the mean strain rate,  $D$  and  $q$  are  
250 material constants which may be taken to be equal to 6700 and 4, respectively, for aluminium  
251 alloy [48].

252 All parameters in Eq. (1) are material constants except for the mean strain rate  $\dot{\epsilon}_m$ , which can  
253 be measured experimentally. The value of the mean strain rate is taken as the average slope  
254 during the rise time which is defined herein as the period when the surface material strain  
255 increases monotonically from zero strain to peak strain. Fig. 8 shows the correlation between  
256 the mean strain rate and the ratio of the impact velocity ( $v_0$ ) and plate thickness ( $t$ ), in units of  
257 m/s and m, respectively. The experimentally measured mean strain rate was observed to be  
258 insensitive to changes in the size of the ice specimen which had diameter varying in the range:  
259 31.8 mm ~ 50.8 mm, but was sensitive to variations in the value of  $v_0$  and  $t$  ( $\dot{\epsilon}_m$  increases with  
260 increasing  $v_0$ , or decreasing  $t$ ). The correlation is approximately linear when plotted to the  
261 logarithmic scale indicating a power law relationship; refer to Eq. (2).

$$262 \quad \dot{\epsilon}_m = 2.09 \left( \frac{v_0}{t} \right)^{0.45} \quad (2)$$



263

264 **Fig. 8. Experimentally measured mean strain rate and its relationship with the velocity of impact and**  
 265 **panel thickness. The spherical ice impactors had diameters of 31.8, 38.1, 44.5, and 50.8 mm.**

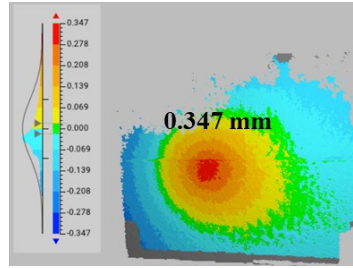
266

267 Consider an imaginary impact scenario of an ice sphere impacting a 4 mm thick aluminium  
 268 panel (5083-H116) at about 46 m/s. The mean strain rate as estimated from Eq. (2) is  $140 \text{ s}^{-1}$ .  
 269 The dynamic flow stress according to Eq. (1) is calculated to be 297 MPa which is almost 1.4  
 270 times higher than the yield strength of the aluminium material (215 MPa). The significance of  
 271 strain rate effects is evident.

### 272 3.3. Indentation profile

273 An optical 3D scanner (*Artec Spider 3D*) was used to scan the dented area on each tested  
 274 (damaged) panel specimen following their impact testing. The scanned images were fused and  
 275 reconstructed into 3D models via the *Artec Studio 15* and *Geomagic Control X* software. Fig.  
 276 9 shows some sample photos and scanned images of the permanent indentation. The presented  
 277 contour maps were constructed by analysing the deformed surface with reference to a flat  
 278 surface.

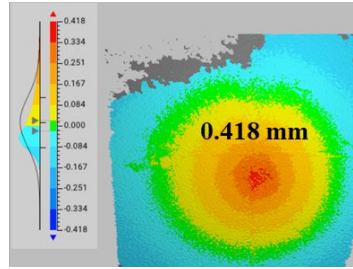
279



280

(a)

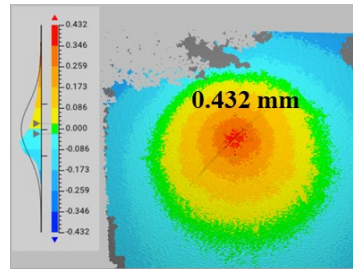
281



282

(b)

283



284

(c)

285 **Fig. 9. Photos and scanned images of the permanent indentation (a) at location L1 (b) at location L5N (c)**  
 286 **at location L5D.**

287 Generalising the shape of indentation and having it expressed in the form of a mathematical  
 288 relationship is the key to indentation modelling. A few assumed, and empirical curve fitted,  
 289 deflection functions as reported in the literature are listed in Table 2. Note, these shape  
 290 functions (as plotted in Fig. 10) were derived from studies of impact scenarios such as blast or  
 291 collision by a large mass. The deflections of the panel in those scenarios are dominated by  
 292 global plastic deformation. Thus, the shape of the indentation of the panel in a hail impact  
 293 scenario might not be represented accurately by any of the listed shape functions.

294

Table 2: Assumed or empirically fitted deflection shape reported in the literature.

No.	Shape function	Comments
1.	$w(r) = w_0 \cos\left(\frac{\pi r}{2R}\right)$	[40]
2.	$w(r) = w_0 \left[0.909 - 2.03 \left(\frac{r}{R}\right)^2 + 1.21 \left(\frac{r}{R}\right)^4\right]$	[40]
3.	$w(r) = w_0 \left[1 - \left(\frac{r}{R}\right)^2\right]$	[40]
4.	$w(r) = w_0 e^{-0.023r}$	[41-43]
5.	$w(r) = w_0 J_0\left(\frac{a \cdot r}{R}\right)$	[47]

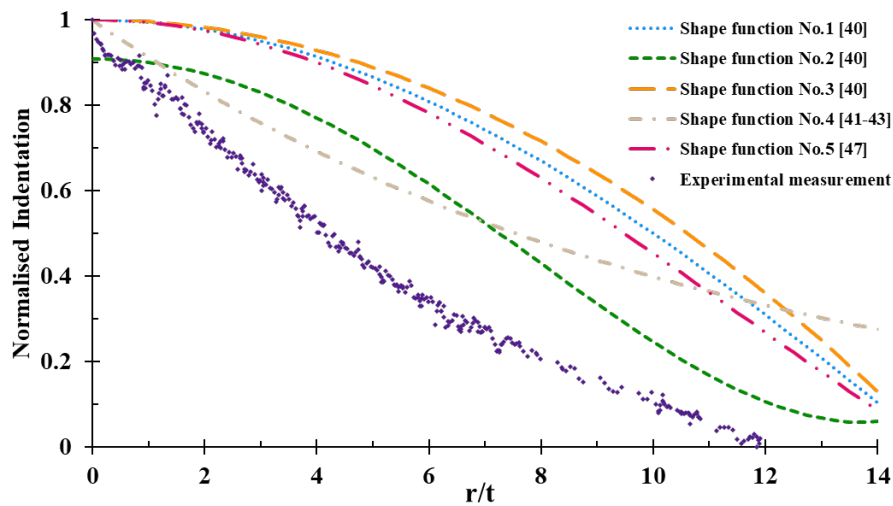


Fig. 10. Comparisons of the shape functions reported in the literature with experimental measurements.

Eq. (3) is proposed herein to generalise the normalised indentation profile of hail impact.

Coefficients in the expression were found by calibration against experimental observations.

$$w(r) = w_0 e^{-b \cdot (r/t)^a} \quad (3)$$

where,  $w(r)$  is the normalised profile of the permanent indentation,  $w_0$  is the maximum

amount of permanent indentation occurring at the impact point,  $r$  is the radial distance

305 measured from the point of impact,  $t$  is the thickness of the aluminium panel, and  $a$  and  $b$  are  
 306 coefficients the values of which can be obtained by calibration against empirical (experimental)  
 307 data.

308 Further analysis of the experimentally measured indentation profile was undertaken by  
 309 extracting the 3D data cloud points to reconstruct the cross-sectional profile at the point of  
 310 impact; refer to Fig. 11. Specific details associated with the eleven sets of experimental data  
 311 used for calibrating the coefficients:  $a$  and  $b$  of Eq. (3) are listed in Table 3. Although the  
 312 location of the point of contact associated with each indentation profile varies between the data  
 313 sets, negligible differences can be seen in their shapes. The calibrated values for parameters  $a$   
 314 and  $b$ , as derived using the Curve Fitting Toolbox in MATLAB, are 1.4 and -0.09, respectively.  
 315 Eq. (3) is accordingly rewritten as Eq. (4).

$$316 \quad w(r) = w_0 e^{-0.09(r/t)^{1.4}} \quad (4)$$

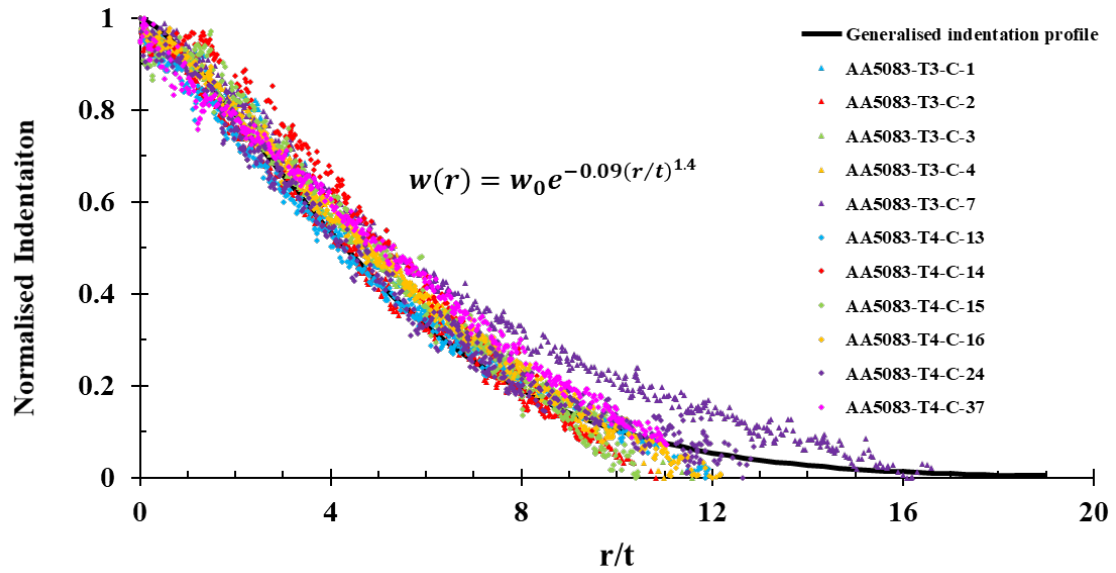
317 As the position of impact was varied the normalised indentation profile across the data sets  
 318 were found to be highly consistent. The diameters of the permanently dented area of the tested  
 319 specimens was found to be within 100 mm, revealing the localised nature of the permanent  
 320 indentation. Thus, Eqs. (3) and (4) are generally applicable to panels of different sizes.

321 **Table 3: 11 sets of experimental data used for studying the indentation profile.**

Test ID	Impact velocity ( $m/s$ )	Panel thickness ( $mm$ )	Impact location	$w_0$ ( $mm$ )
AA5083-T3-C-1	46.88	3	L1	0.480
AA5083-T3-C-2	51.49	3	L2N	0.608
AA5083-T3-C-3	50.35	3	L2D	0.598
AA5083-T3-C-4	54.46	3	L3N	0.664
AA5083-T3-C-7	44.45	3	L3D	0.483
AA5083-T4-C-13	78.25	4	L1	0.451
AA5083-T4-C-14	73.09	4	L2N	0.375
AA5083-T4-C-15	76.92	4	L2D	0.391

AA5083-T4-C-16	77.30	4	L3N	0.466
AA5083-T4-C-24	64.33	4	L4N	0.283
AA5083-T4-C-37	79.10	4	L5D	0.525

322



323

324  
325

Fig. 11. Normalised indentation profile measured experimentally and estimated from empirical equation Eq. (4).

## 326 4. Analytical Model Development

327 This section presents the conception and development of an analytical model for predicting the  
328 maximum permanent indentation into an aluminium cladding panel induced by hail impact.  
329 Section 4.1 demonstrates the fundamentals of quantifying the amount of energy expended in  
330 plastic straining for a given amount of (initial) kinetic energy delivered by the impact. The  
331 derivation and validation of the algebraic predictive relationship are presented in Section 4.2,  
332 along with an extra note in Section 4.3.

### 333 4.1. Energy expended in plastic straining

334 The total amount of energy expended in plastic straining causing permanent indentation into  
335 the metal ( $W_p$ ), referred to herein as “plastic work”, can be expressed as the volume integral of  
336 the sum of the product of radial and circumferential stresses and their respective strains as  
337 presented in Eq. (5). The equality was derived from thin plate theory and was based on the  
338 assumption of plane stress and symmetric conditions (i.e., the *Kirchhoff* assumption). The  
339 stated assumptions can be justified by reference to the experimental observations as presented  
340 in Section 3.1.

$$341 \quad W_p = \int_{vol} [\int (\sigma_r d\varepsilon_r + \sigma_\theta d\varepsilon_\theta)] dV \quad (5)$$

342 where,  $W_p$  is the plastic work, and  $\sigma_r$ ,  $\sigma_\theta$ ,  $\varepsilon_r$ , and  $\varepsilon_\theta$  are the stresses and strains in the radial  
343 and circumferential directions, respectively.

344 The relevant strains can be found using Eqs. (6a) and (6b) below.

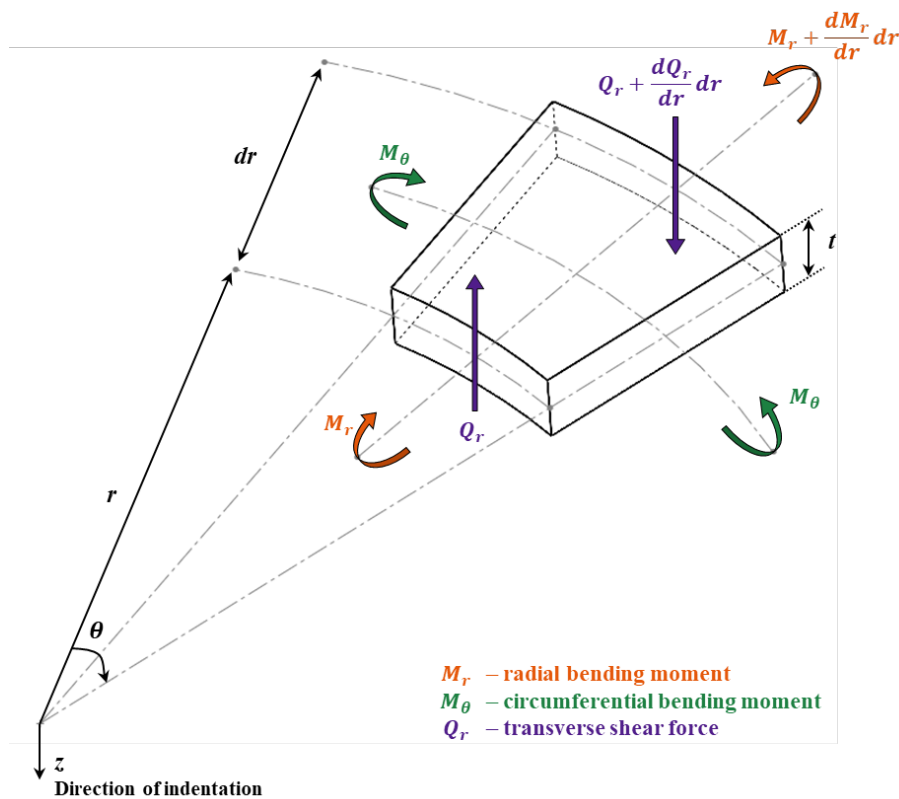
$$345 \quad \varepsilon_r = \varepsilon_m + \varepsilon_{rb} = \frac{1}{2} \left( \frac{\partial w}{\partial r} \right)^2 + Z\kappa_r \quad (6a)$$

$$346 \quad \varepsilon_\theta = \varepsilon_{\theta b} = Z\kappa_\theta \quad (6b)$$

347 where,  $\varepsilon_m$ ,  $\varepsilon_{rb}$ , and  $\varepsilon_{\theta b}$  are the radial membrane strain, radial bending strain, and  
 348 circumferential bending strains respectively;  $z$  represents the direction of indentation  
 349 (transverse) in a cylindrical coordinate system as depicted in Fig. 12;  $\kappa_r$  and  $\kappa_\theta$  are the radial  
 350 and circumferential curvatures as expressed in Eqs. (7a) and (7b).

351 
$$\kappa_r = -\frac{\partial^2 w}{\partial r^2} \tag{7a}$$

352 
$$\kappa_\theta = -\frac{1}{r} \frac{\partial w}{\partial r} \tag{7b}$$



353

354 **Fig. 12. Cylindrical coordinate system and notation used in this study.**

355

356 The magnitude of various stresses that are developed in the radial and circumferential  
 357 directions can be found using the presented relationships along with Eq. (1) which provides an  
 358 estimate for the mean dynamic flow stress  $\sigma_d$ . The total amount of plastic work can be found

359 by the substitution of Eqs. (1), (6) – (7) into Eq. (5). The result of the substitution can be  
 360 expressed in the form of Eq. (8).

$$361 \quad W_p = W_m + W_{rb} + W_{\theta b} = \int_{vol} \sigma_d (\varepsilon_m + \varepsilon_{rb} + \varepsilon_{\theta b}) dV \quad (8)$$

362 where,  $W_m$ ,  $W_{rb}$ , and  $W_{\theta b}$  are the plastic work components attributed to the radial membrane  
 363 force (stress), radial bending moments, and circumferential bending moments, respectively.  
 364 The full expressions for all three plastic work terms are shown in Eqs. (9a) – (9c).

$$365 \quad W_m = \pi \sigma_d t \int_0^R \left( \frac{\partial w}{\partial r} \right)^2 r dr \quad (9a)$$

$$366 \quad W_{rb} = \frac{1}{2} \pi \sigma_d t^2 \int_0^R \left( -\frac{\partial^2 w}{\partial r^2} r \right) dr \quad (9b)$$

$$367 \quad W_{\theta b} = \frac{1}{2} \pi \sigma_d t^2 \int_0^R \left( -\frac{\partial w}{\partial r} \right) dr \quad (9c)$$

368 where,  $R$  is the radial distance measured from the point of impact to the edge of the dented area,  
 369 and  $w$  is the indentation profile as defined by Eq. (4).

370 Substituting Eq. (4) into Eqs. (9a) – (9c) gives Eqs. (10a) – (10c) for quantifying the respective  
 371 components of the plastic work. Note that  $\gamma$  represents the lower incomplete gamma function.

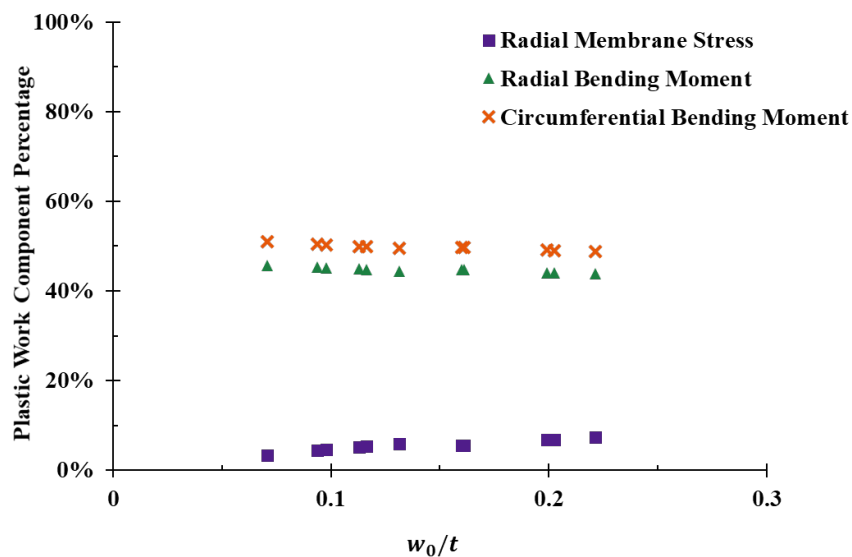
$$372 \quad W_m = \frac{7}{20} \pi \sigma_d t w_0^2 \left\{ 1 - \gamma \left[ 2, 0.18 \left( \frac{R}{t} \right)^{1.4} \right] \right\} \quad (10a)$$

$$373 \quad W_{rb} = \frac{1}{2} \pi \sigma_d t^2 w_0 \left\{ 1.4 \gamma \left[ 2, 0.09 \left( \frac{R}{t} \right)^{1.4} \right] - 0.4 \exp \left[ -0.09 \left( \frac{R}{t} \right)^{1.4} \right] - 1 \right\} \quad (10b)$$

$$374 \quad W_{\theta b} = \frac{1}{2} \pi \sigma_d t^2 w_0 \left\{ 1 - \exp \left[ -0.09 \left( \frac{R}{t} \right)^{1.4} \right] \right\} \quad (10c)$$

375 Fig. 13 shows the percentage contribution to the total plastic work ( $W_p$ ) by each of the three  
 376 components ( $W_m$ ,  $W_{rb}$ , and  $W_{\theta b}$ ), as found using Eqs. (10a) – (10c). The presented results were  
 377 derived from a diversity of impact scenarios as characterised by the indentation-to-thickness

378 ratio ( $w_0/t$ ). It is shown that the amount of plastic work done by the radial and circumferential  
 379 bending moments were the main contributors to energy absorption by the aluminium panel. As  
 380 the intensity of impact was increased (i.e., when  $w_0/t$  became higher) the amount of  
 381 contribution from the radial membrane forces (and stresses) was increased. Contributions by  
 382 bending were reduced. It is noted that in a hail impact scenario, the level of intensity is  
 383 generally small. The amount of indentation is typically less than the thickness of the panel, as  
 384 shown in Table 3. In summary, the assumption of neutral midplane and the application of plate  
 385 bending theory is generally valid for dealing with the impact action of hail. Should there be a  
 386 situation where the amount of indentation exceeds the panel thickness ( $w_0/t > 1$ ), the amount  
 387 of plastic work done which is attributed to membrane action can become the dominant source  
 388 of energy dissipation, as reported in the literature [49, 50].



389

390 **Fig. 13. Comparison of the plastic work component done by radial membrane stress, radial bending**  
 391 **moment, and circumferential bending moment in different impact scenarios.**

392

393 Table 4 summarises the total amount of plastic work consumed in each of the tested scenarios  
 394 as calculated using Eqs. (8), (10a) – (10c), and the amount of kinetic energy delivered by the  
 395 impact, as shown in Table 3. The plastic work to kinetic energy ratios are also listed.

396  
397

**Table 4: Summary of the total plastic work, initial kinetic energy, and plastic work to kinetic energy ratio.**

Test ID	Total plastic work $W_p$ (J)	Initial kinetic energy $KE_0$ (J)	$\frac{W_p}{KE_0}$
AA5083-T3-C-1	4.02	64.84	6.21%
AA5083-T3-C-2	5.17	78.22	6.61%
AA5083-T3-C-3	5.08	76.06	6.68%
AA5083-T3-C-4	5.68	88.96	6.38%
AA5083-T3-C-7	4.06	59.27	6.85%
		<b>Average</b>	<b>6.55%</b>
AA5083-T4-C-13	3.83	180.62	2.12%
AA5083-T4-C-14	3.15	157.59	2.00%
AA5083-T4-C-15	3.29	174.56	1.89%
AA5083-T4-C-16	3.95	176.27	2.24%
AA5083-T4-C-24	2.35	122.09	1.93%
AA5083-T4-C-37	4.49	187.68	2.39%
		<b>Average</b>	<b>2.09%</b>

398

399 The plastic work and initial kinetic energy values as recorded from the impact experiments (as  
400 listed in Table 4) can be summarised into Eqs. (11a) and (11b).

401  $\frac{W_p}{KE_0} \Big|_{t=3\text{ mm}} \approx 6.55\%$  for a plate with a thickness of 3 mm (11a)

402  $\frac{W_p}{KE_0} \Big|_{t=4\text{ mm}} \approx 2.09\%$  for a plate with a thickness of 4 mm (11b)

403 The value of  $W_p$  may be estimated conveniently using Eqs. (11a) and (11b) for impact  
404 scenarios where the initial kinetic energy (mass-velocity combination) delivered by the  
405 impactor is known.

406 **4.2. An algebraic expression for determining the permanent indentation**

407 Substituting Eqs. (10a) – (10c) into Eq. (8) and rearranging the terms gives Eq. (12) which  
408 provides predictions for the value of  $w_0$ .

$$\begin{aligned}
409 \quad w_0 &= \frac{1}{2} \left( -t \frac{B}{A} + \sqrt{t^2 \frac{B^2}{A^2} + \frac{4W_p}{\pi \sigma_d t A}} \right) \\
410 \quad - \quad A &= 0.35 \left\{ 1 - \gamma \left[ 2, 0.18 \left( \frac{R}{t} \right)^{1.4} \right] \right\} \\
411 \quad - \quad B &= \left\{ 1 - 0.3 \exp \left[ -0.09 \left( \frac{R}{t} \right)^{1.4} \right] - 0.7\gamma \left[ 2, 0.09 \left( \frac{R}{t} \right)^{1.4} \right] \right\} \quad (12)
\end{aligned}$$

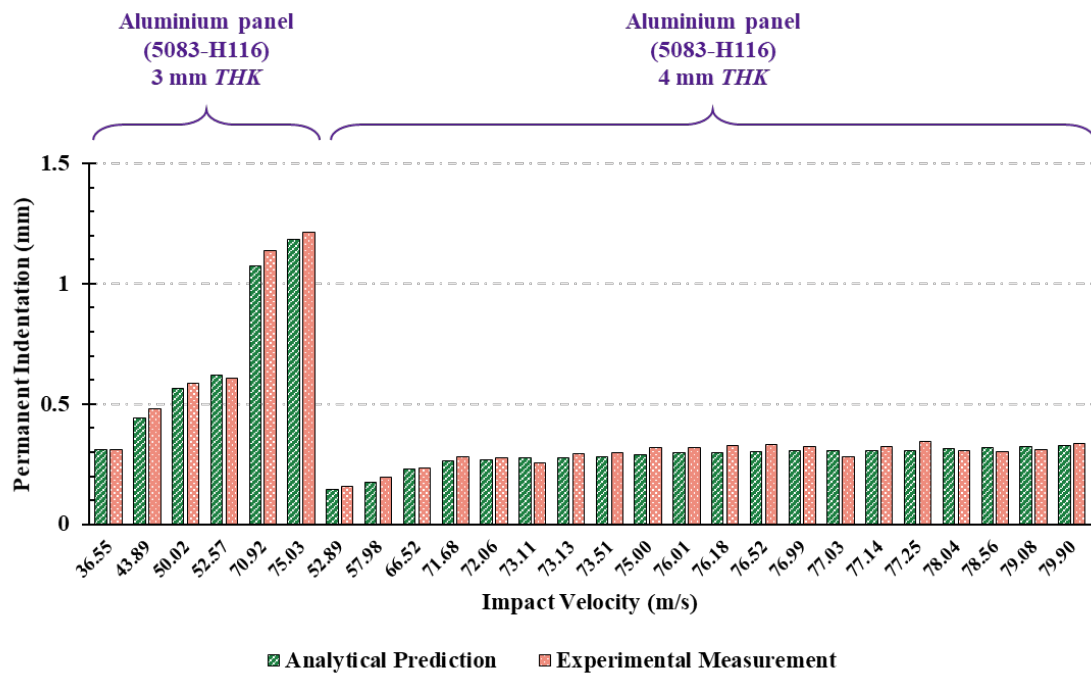
412 Note, the value of  $R$  may be treated as a constant, and is taken as 50 mm, which is the maximum  
413 radius of the dented area on the aluminium panel as observed from the experiments conducted  
414 by the authors. Coefficients  $A$  and  $B$  are also constants for a given thickness ( $t$ ) of the panel.  
415 These values of the coefficients for two common panel thicknesses are listed in Table 5.

416 **Table 5: Numerical values of  $A$  and  $B$  for panels with a thickness of 3 mm and 4 mm.**

Aluminium panel thickness ( $mm$ )	$A$	$B$
3	0.3499	0.9422
4	0.3454	0.7743

417  
418 In summary, the amount of permanent indentation into the aluminium plate ( $w_0$ ) can be  
419 predicted with the combined use of Eqs. (1), (2), (11a) or (11b), and (12), when the size (mass)  
420 of the hail, the velocity of impact, the thickness and grade of the target aluminium panels are  
421 well defined. The accuracy of the proposed analytical expression (Eq. (12)) has been validated  
422 by comparisons against an additional twenty-six sets of experimentally measured permanent  
423 indentations that are different to the results listed in Table 3 (that were employed in the  
424 calibration of the coefficients). Thus, the experimental results involved in the comparison are  
425 therefore independent of the calibration process. Comparisons of the predictions against these  
426 independent measurements are presented in Fig. 14 for impact scenarios across different panel  
427 thicknesses and impact velocities. Numerical discrepancies between the predicted results from

428 Eq. (12) and experimental measurements were all within 10%. The outcome of the comparison  
 429 assures the accuracy of the proposed hand calculation procedure.



430

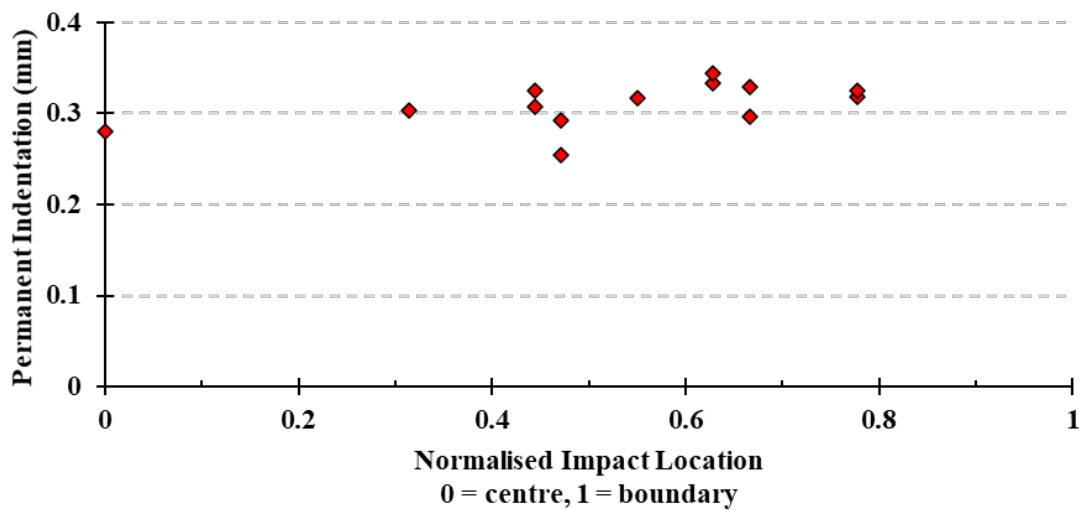
431 Fig. 14. Comparison of permanent indentations predicted by the analytical expression and experimentally  
 432 measured by the optical 3D scanner.

433

### 434 4.3. A note on the spatial variance of indentation

435 In an earlier investigation employing metal impactors, the amount of permanent indentation  
 436 into the aluminium panel was reported to be increasing with decreasing distance between the  
 437 impact position and the closest supporting edge of the panel [44, 51]. Interestingly, this spatial  
 438 variation was not observed in the current study which deals with hail impact. The reason is that  
 439 the amount of permanent indentation generated by the impact of ice was too small to be  
 440 captured. Fig. 15 shows comparisons of some experimentally measured permanent indentations  
 441 against different locations of impact when the impact velocity was kept unchanged. There is a  
 442 weak trend showing the amount of indentation to increase slightly impact position moves closer  
 443 to the supporting edge of the panel. However, the observed variation was too minor to warrant

444 it incorporated into the analytical model. The amount of variation is also controlled by the yield  
445 strength of the alloy. The 5083-H116 (215 MPa) alloy adopted in this study is believed to have  
446 suppressed the spatial variation because of its higher yield strength in comparison with other  
447 alloy grades such as 5005-H34 (105 MPa) and 5052-H32 (160 MPa).



448

449 Fig. 15. Spatial variance of permanent indentation measured experimentally at different locations on the  
450 targeted panel.

451

## 452 5. Application of the Proposed Analytical Predictive Relationships

453 The application of the developed analytical model for the prediction of permanent indentation  
454  $w_0$  is demonstrated in this section. The considered impact scenario was a hailstone of 50.8 mm  
455 in diameter weighing 59.5 g, impacting an aluminium cladding panel with an incident velocity  
456 of 50 m/s. The targeted panel, which was fully clamped on all four edges, had dimensions of  
457 900 mm  $\times$  900 mm  $\times$  3 mm thick, and was fabricated of alloy grade 5083-H116. The yield  
458 strength of this grade was taken as 215 MPa.

459 Solution:

460 The mean strain rate ( $\dot{\epsilon}_m$ ) which is estimated using Eq. (2) is substituted into Eq. (1) for  
 461 calculation of the dynamic flow stress ( $\sigma_d$ ).

$$462 \quad \dot{\epsilon}_m = 2.09 \left( \frac{v_0}{t} \right)^{0.45} = 2.09 \left( \frac{50}{0.003} \right)^{0.45} = 166 \text{ s}^{-1}$$

$$463 \quad \sigma_d = \sigma_y \left[ 1 + \left( \frac{\dot{\epsilon}_m}{D} \right)^{\frac{1}{q}} \right] = 215 \left[ 1 + \left( \frac{166}{6700} \right)^{\frac{1}{4}} \right] = 300 \text{ MPa}$$

464 Eq. (11a) is then made use of for predicting the amount of energy ( $W_p$ ) expended in causing  
 465 permanent indentation. Results so obtained are then substituted into Eq. (12) for determination  
 466 of the maximum indentation ( $w_0$ ).

$$467 \quad w_0 = \frac{1}{2} \left( -t \frac{B}{A} + \sqrt{t^2 \frac{B^2}{A^2} + \frac{4W_p}{\pi \sigma_d t A}} \right)$$

$$468 \quad = \frac{1}{2} \left( -0.003 \frac{0.9422}{0.3499} + \sqrt{0.003^2 \frac{0.9422^2}{0.3499^2} + \frac{4 \times 4.87}{\pi (300 \times 10^6) (0.003) (0.3499)}} \right)$$

$$469 \quad = 0.57 \text{ mm}$$

470 The model prediction of 0.57 mm is compared against the experimental measurement of 0.59  
 471 mm demonstrating good consistency. Prediction-measurement comparisons across a range of  
 472 impact scenarios can be found in Fig. 14.

## 473 6. Conclusion

474 A new algebraic expression for predicting the amount of permanent indentation into the surface  
475 of an aluminium alloy panel generated by the impact of hail has been developed in this study.  
476 The strain rate effect has been incorporated to account for the hardening behaviour of the  
477 aluminium material when subject to a highly transient action of hail impact (of duration  $\sim 1$   
478 ms). A generalised shape function has been developed to model the unique curvature and shape  
479 of the indentation profile on the surface of the aluminium panel. The amount of energy  
480 absorbed by the plate in forming the indentation was found to consume only a tiny fraction of  
481 the (initial) kinetic energy delivered by the impact (with 6.55% and 2.09% for plate thicknesses  
482 of 3 mm and 4 mm, respectively). In impact scenarios where the amount of indentation was  
483 less than the plate thickness, radial and circumferential flexural actions consumed most of the  
484 energy, whereas contributions from membrane actions were minor. Predictions from the  
485 proposed analytical expression for the considered impact scenarios were all within 10% of the  
486 experimentally measured results. Accurate predictions of the amount of indentation can be  
487 made once the following parameters are known: size (mass) of the hail, velocity of impact,  
488 thickness and grade (yield strength) of the alloy. The outcome of the current study enables  
489 damage to cladding panels in projected hail impact scenarios to be predicted accurately without  
490 the need for any costly impact experimentations.

491 **CRedit authorship contribution statement**

492 **Shuangmin Shi:** Methodology, Investigation, Data curation, Formal analysis, Validation,  
493 Visualization, Writing – Original Draft, Writing – Review & Editing. **Nelson Lam:**  
494 Conceptualization, Writing – Review & Editing, Supervision, Funding acquisition. **Yiwen Cui:**  
495 Investigation, Data curation, Formal analysis. **Guoxing Lu:** Conceptualization, Methodology,  
496 Resources, Funding acquisition. **Emad Gad:** Conceptualization, Funding acquisition. **Lihai**  
497 **Zhang:** Conceptualization, Methodology, Writing – Review & Editing, Supervision, Funding  
498 acquisition, Project administration.

499

500 **Declaration of competing interest**

501 The authors declare that they have no known competing financial interests or personal  
502 relationships that could have appeared to influence the work reported in this paper.

503

504 **Acknowledgements**

505 This work is financially supported by the Australian Research Council Linkage Project (ARC  
506 LP190100208). Cash and in-kind support by Mr Ian Bennie (General Manager of *Ian Bennie*  
507 *and Associates*) and Mr Suresh Sutrave (Director of *Atlite Skylights*) as Partner Investigators  
508 of the linkage project are gratefully acknowledged. The authors are also grateful to Mr  
509 Kubendra Rao, Mr Jasman Anwar and Mrs Josie Stokoe for their kind help in the preparation  
510 of the test apparatus. The authors wish to thank Dr Shanqing Xu, Mrs Cong Wang and Ms Jia  
511 Ming Goh for their generous support during the experiment.

512

513

## 514 References

- 515 1. Minor, J.E., *Windborne debris and the building envelope*. Journal of Wind Engineering  
516 and Industrial Aerodynamics, 1994. **53**(1-2): p. 207-227.
- 517 2. Sparks, P., *Wind speeds in tropical cyclones and associated insurance losses*. Journal  
518 of wind engineering and industrial aerodynamics, 2003. **91**(12-15): p. 1731-1751.
- 519 3. Sparks, P.R., S. Schiff, and T. Reinhold, *Wind damage to envelopes of houses and*  
520 *consequent insurance losses*. Journal of wind engineering and industrial aerodynamics,  
521 1994. **53**(1-2): p. 145-155.
- 522 4. Changnon, S.A., *Temporal and spatial distributions of damaging hail in the continental*  
523 *United States*. Physical Geography, 2008. **29**(4): p. 341-350.
- 524 5. Changnon, S.A., D. Changnon, and S.D. Hilberg, *Hailstorms across the nation: An*  
525 *atlas about hail and its damages*. ISWS Contract Report CR-2009-12, 2009.
- 526 6. Ali, M., et al., *Simple hand calculation method for estimating deflection generated by*  
527 *the low velocity impact of a solid object*. Australian Journal of Structural Engineering,  
528 2014. **15**(3): p. 243-259.
- 529 7. Yang, Y., N. Lam, and L. Zhang, *Evaluation of simplified methods of estimating beam*  
530 *responses to impact*. International Journal of Structural Stability and Dynamics, 2012.  
531 **12**(03): p. 1250016.
- 532 8. Yang, Y., N. Lam, and L. Zhang, *Estimation of response of plate structure subject to*  
533 *low velocity impact by a solid object*. International journal of structural stability and  
534 dynamics, 2012. **12**(06): p. 1250053.
- 535 9. Yang, Y., et al., *Simplified analysis of low velocity impact actions on shallow domes*.  
536 International Journal of Applied Mechanics, 2013. **5**(02): p. 1350013.
- 537 10. Standard, B., *Eurocode 1: Actions on structures—*. 2010.
- 538 11. Perera, S., et al., *Deterministic solutions for contact force generated by impact of*  
539 *windborne debris*. International Journal of Impact Engineering, 2016. **91**: p. 126-141.
- 540 12. Sun, J., et al., *Contact forces generated by fallen debris*. Structural Engineering and  
541 Mechanics, 2014. **50**(5): p. 589-603.
- 542 13. Sun, J., et al., *Contact forces generated by hailstone impact*. International Journal of  
543 Impact Engineering, 2015. **84**: p. 145-158.
- 544 14. Sun, J., et al., *Computer simulation of contact forces generated by impact*. International  
545 Journal of Structural Stability and Dynamics, 2017. **17**(01): p. 1750005.
- 546 15. Sun, J., et al., *A note on Hunt and Crossley model with generalized visco-elastic*  
547 *damping*. International Journal of Impact Engineering, 2018. **121**: p. 151-156.
- 548 16. Yang, Y., et al., *An innovative procedure for estimating contact force during impact*.  
549 International Journal of Applied Mechanics, 2014. **6**(06): p. 1450079.
- 550 17. Chen, S., et al., *Experiments on an ice ball impacting onto a rigid target*. International  
551 Journal of Impact Engineering, 2022. **167**: p. 104281.
- 552 18. Shi, S., et al., *An analytical approach for modelling contact forcing function of*  
553 *hailstone impact*. International Journal of Solids and Structures, 2023. **269**: p. 112214.

- 554 19. Saini, D. and B. Shafei, *Prediction of extent of damage to metal roof panels under hail*  
555 *impact*. Engineering Structures, 2019. **187**: p. 362-371.
- 556 20. Tang, Z., et al., *Numerical and experimental investigation on hail impact on composite*  
557 *panels*. International Journal of Impact Engineering, 2017. **105**: p. 102-108.
- 558 21. Kim, H., D.A. Welch, and K.T. Kedward, *Experimental investigation of high velocity*  
559 *ice impacts on woven carbon/epoxy composite panels*. Composites Part A: applied  
560 science and manufacturing, 2003. **34**(1): p. 25-41.
- 561 22. Park, H. and H. Kim, *Damage resistance of single lap adhesive composite joints by*  
562 *transverse ice impact*. International Journal of Impact Engineering, 2010. **37**(2): p. 177-  
563 184.
- 564 23. Wu, X., et al., *Dynamic responses and energy absorption of sandwich panel with*  
565 *aluminium honeycomb core under ice wedge impact*. International Journal of Impact  
566 Engineering, 2022. **162**: p. 104137.
- 567 24. Rhymer, J., H. Kim, and D. Roach, *The damage resistance of quasi-isotropic*  
568 *carbon/epoxy composite tape laminates impacted by high velocity ice*. Composites Part  
569 A: Applied Science and Manufacturing, 2012. **43**(7): p. 1134-1144.
- 570 25. Cai, W., L. Zhu, and X. Qian, *Dynamic responses of steel plates under repeated ice*  
571 *impacts*. International Journal of Impact Engineering, 2022. **162**: p. 104129.
- 572 26. Cai, W., et al., *Numerical simulations for plates under ice impact based on a concrete*  
573 *constitutive ice model*. International journal of impact engineering, 2020. **143**: p.  
574 103594.
- 575 27. Herbin, A. and M. Barbato, *Fragility curves for building envelope components subject*  
576 *to windborne debris impact*. Journal of Wind Engineering and Industrial  
577 Aerodynamics, 2012. **107**: p. 285-298.
- 578 28. Alphonso, T. and M. Barbato, *Experimental fragility curves for aluminum storm panels*  
579 *subject to windborne debris impact*. Journal of Wind Engineering and Industrial  
580 Aerodynamics, 2014. **134**: p. 44-55.
- 581 29. Chen, W., H. Hao, and H. Du, *Failure analysis of corrugated panel subjected to*  
582 *windborne debris impacts*. Engineering Failure Analysis, 2014. **44**: p. 229-249.
- 583 30. Carney, K.S., et al., *A phenomenological high strain rate model with failure for ice*.  
584 International Journal of Solids and Structures, 2006. **43**(25-26): p. 7820-7839.
- 585 31. Tippmann, J.D., H. Kim, and J.D. Rhymer, *Experimentally validated strain rate*  
586 *dependent material model for spherical ice impact simulation*. International journal of  
587 impact engineering, 2013. **57**: p. 43-54.
- 588 32. Pernas-Sánchez, J., et al., *Numerical modeling of ice behavior under high velocity*  
589 *impacts*. International Journal of Solids and Structures, 2012. **49**(14): p. 1919-1927.
- 590 33. Liu, K., P. Li, and Z. Wang, *A rate-sensitive and pressure-dependent failure criterion*  
591 *for hail ice*. International Journal of Impact Engineering, 2022. **168**: p. 104291.
- 592 34. Cui, Q. and J. Yang, *Evaluation of numerical simulation methods and ice material*  
593 *models for intermediate-velocity hail impact simulation*. Engineering Structures, 2021.  
594 **244**: p. 112831.

- 595 35. Jones, N., *A theoretical study of the dynamic plastic behavior of beams and plates with*  
596 *finite-deflections*. International Journal of Solids and Structures, 1971. **7**(8): p. 1007-  
597 1029.
- 598 36. Jones, N., *On the mass impact loading of ductile plates*. Defence Science Journal, 2003.  
599 **53**(1): p. 15.
- 600 37. Jones, N., S.-B. Kim, and Q. Li, *Response and failure of ductile circular plates struck*  
601 *by a mass*. 1997.
- 602 38. Lu, G. and T. Yu, *Energy absorption of structures and materials*. 2003: Elsevier.
- 603 39. Jones, N., *Impact loading of ductile rectangular plates*. Thin-walled structures, 2012.  
604 **50**(1): p. 68-75.
- 605 40. Duffey, T.A., *Large deflection dynamic response of clamped circular plates subjected*  
606 *to explosive loading*. 1967, Sandia Corp., Albuquerque, N. Mex.
- 607 41. Calder, C.A. and W. Goldsmith, *Plastic deformation and perforation of thin plates*  
608 *resulting from projectile impact*. International Journal of Solids and Structures, 1971.  
609 **7**(7): p. 863-881.
- 610 42. Mohotti, D., et al., *Out-of-plane impact resistance of aluminium plates subjected to low*  
611 *velocity impacts*. Materials & Design, 2013. **50**: p. 413-426.
- 612 43. Pathirana, M., et al., *Damage modelling of aluminium panels impacted by windborne*  
613 *debris*. Journal of Wind Engineering and Industrial Aerodynamics, 2017. **165**: p. 1-12.
- 614 44. Shi, S., et al., *Indentation into an aluminium panel by the impact of a rigid spherical*  
615 *object*. Thin-Walled Structures, 2022. **180**: p. 109935.
- 616 45. Liu, B., R. Villavicencio, and C.G. Soares, *On the failure criterion of aluminum and*  
617 *steel plates subjected to low-velocity impact by a spherical indenter*. International  
618 Journal of Mechanical Sciences, 2014. **80**: p. 1-15.
- 619 46. Bennie, I., *Advice sought from personal communication in 2021 with Ian Bennie of Ian*  
620 *Bennie & Associates which is the National Association of Testing Authorities (NATA)*  
621 *sole accredited testing laboratory in Australia*. 2021.
- 622 47. Gharababaei, H. and A. Darvizeh, *Experimental and Analytical Investigation of Large*  
623 *Deformation of Thin Circular Plates Subjected to Localized and Uniform Impulsive*  
624 *Loading*. Mechanics based design of structures and machines, 2010. **38**(2): p. 171-  
625 189.
- 626 48. Jones, N., *Structural impact*. 2011: Cambridge university press.
- 627 49. Li, D., et al., *Energy absorption of aluminum panels subjected to gelatin projectile*  
628 *impact*. Latin American Journal of Solids and Structures, 2019. **16**.
- 629 50. Zaera, R., A. Arias, and C. Navarro, *Analytical modelling of metallic circular plates*  
630 *subjected to impulsive loads*. International journal of solids and structures, 2002. **39**(3):  
631 p. 659-672.
- 632 51. Shah, Q.H. and Y.A. Abakr, *Effect of distance from the support on the penetration*  
633 *mechanism of clamped circular polycarbonate armor plates*. International Journal of  
634 Impact Engineering, 2008. **35**(11): p. 1244-1250.
- 635